EES Catalysis

PAPER

View Article Online
View Journal | View Issue

Cite this: *EES Catal.*, 2025, 3, 152

Unidirectional bubble transportation on slippery micro-cone array electrodes enables spontaneous 99.99% gas separation in membrane-less water electrolysis†

Linfeng Yu,‡[a] Yingze Yang,‡[a] Pengpeng Xie,‡[a] Qingzhen Xu,[a] Anuj Kumar,[c] Liang Luo,*[a] Hui Li,[d] Haijun Xu,[a] Haohong Duan*[b] and Xiaoming Sun*[a]

Received 3rd September 2024,
Accepted 18th November 2024

DOI: 10.1039/d4ey00184b

rsc.li/eescatalysis

Membrane-less electrolysis is utilized for many gaseous chemical productions. However, the problems of gas mixing and low energy efficiency remain huge obstacles for its practical application. Herein, we have prepared a biomimetic electrode by three-dimensional (3D) printing technology, featuring a "slippery aerophobic" surface and micro-cone array structure with tunable tilting angles. These electrodes enable the bubbles that are generated at the cone tip to "roll-up" rapidly along the electrode towards its base, rather than being directly released into the electrolyte, resulting in gas mixing. The unidirectional bubble transportation behavior was understood by a collective analysis of the Laplace pressure on cones, bubble buoyancy and irreversible hysteresis. As a proof of concept, we employed this biomimetic electrode in membrane-less water electrolysis. At a current density of 240 mA cm^{-2}, we achieved the separation of H_2 and O_2 gases with >99.99% purity even with an electrode distance as short as 1.5 mm. This work demonstrated the efficiency of precisely manipulating bubble transportation in membrane-less electrolysis that does not rely on expensive membranes.

Broader context

Membrane-less electrolyzers have attracted a tremendous amount of attention, particularly as promising alternatives for harsh electrolysis systems such as hypochlorite, NF_3 or SF_6 production, where membrane durability and maintenance are significant challenges. To guarantee the purity of gas production, the inter-electrode distance has to be set long enough, resulting in increased energy consumption owing to diffusion resistance. Herein, we propose a tilted micro-cone array (TMCA) electrode with a unique slippery aerophobic surface, to enable unidirectional bubble transportation along the electrode surface in a "rolling-up" manner. Taking water splitting as a probe reaction, this approach enables spontaneous gas separation (>99.9%) at an anode/cathode distance as short as 1.5 mm at high current density, providing an energy-efficient and sustainable solution for membrane-less electrolysis. Our findings highlight the critical role of precise bubble manipulation on electrodes, presenting new opportunities for spontaneous gas transportation in membrane-less electrolysis systems.

Introduction

Membrane-less electrolyzers have become promising candidates for various electrolysis systems, particularly in harsh conditions (*e.g.* the production of hypochlorite, NF_3 or SF_6),[1,2] owing to concerns about membrane durability and corresponding maintenance issues. While the production of gases with high purity is a precondition of downstream applications, as well as a reduction in the cost and energy required for subsequent gas separation.[3] To ensure the strict separation of gaseous products (>99.99%) in such membrane-less electrolysis, elongation of the anode/cathode distance[4–6] or fluid and shearing action[7] have to be carefully adjusted. However, both solutions would increase electrolysis energy consumption due to the increased diffusion resistance or costs in manipulating the flow field in addition to electrochemical reactions.[8,9]

It has recently been recognized that electrode structural engineering is vital for the promotion of electrolysis efficiency, besides optimization of catalyst composition.[10–13] For example,

[a] State Key Laboratory of Chemical Resource Engineering, College of Chemistry, Beijing University of Chemical Technology, Beijing 100029, China. E-mail: luoliang@mail.buct.edu.cn, sunxm@mail.buct.edu.cn
[b] Department of Chemistry, Tsinghua University, Beijing 100084, China
[c] Institute of Humanities and Applied Science, Department of Chemistry, GLA University, Mathura 281406, India
[d] Beijing Advanced Innovation Center for Soft Matter Science and Engineering, Beijing University of Chemistry Technology, Beijing 100029, China

† Electronic supplementary information (ESI) available. See DOI: https://doi.org/10.1039/d4ey00184b

‡ These authors contributed equally to this work.

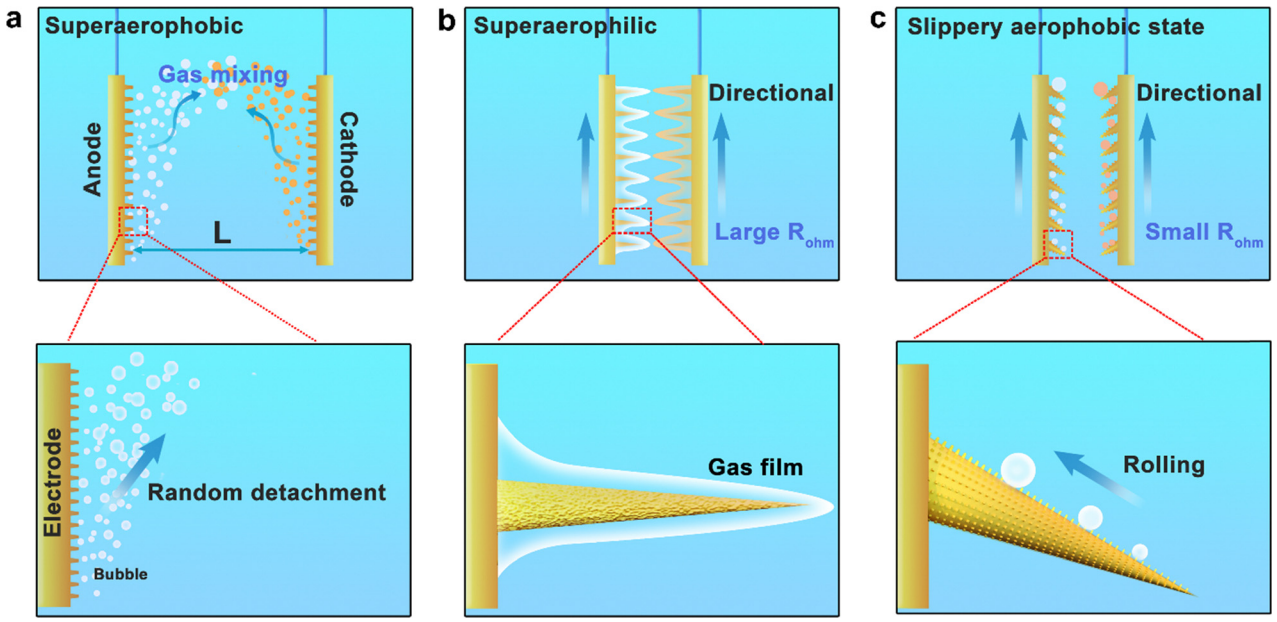

Fig. 1 Schematic diagram of the movement of bubbles on different electrodes. (a) Schematic illustration of conventional superaerophobic electrodes, where gases detach randomly with a higher probability of gas mixing. (b) Schematic illustration of superaerophilic electrodes, where a gas film blocks the reaction active site, inducing large ohmic resistance (R_{ohm}). (c) Schematic illustration of slippery aerophobic electrodes, which can efficiently transport the directional gas bubbles in a "rolling-up" manner, with small ohmic resistance (R_{ohm}).

superaerophobic nanoarray electrodes have shown superior performance in promoting GER performance by means of accelerating bubble detachment and lowering diffusion resistance. However, gas mixing might be even more serious than in traditional membrane-less electrolysis when superaerophobic electrodes are used, because the smaller bubbles generated are more easily suspended and have a longer random motion distance (Fig. 1a). Therefore, the unidirectional transportation of self-driven bubbles based on electrode surface structural engineering is highly desirable but challenging.

Recently, biomimetic structural engineering has received increasing attention for underwater bubble collection, and manipulation,[14–20] as well as droplet transportation. Feng *et al.* utilized an asymmetric pine needle structure and cleverly applied the tip-induced flip (TIF) effect to direct and secure the droplets on the curved side of a pillar.[21] Yao *et al.* developed superaerophilic (superhydrophobic) coatings with micro/nano hierarchies, which enable spontaneous bubble splitting along open channels.[22] In particular, superaerophilic surfaces have been well documented in many studies for manipulating underwater bubble adhesion and "slippery" transportation properties, basically utilizing the shape or wettability gradient, including 1D and 2D transportation and combinations with other different control strategies[18,21–26] (Fig. 1b). Recently, to avoid the common strong adhesion of gaseous products and delayed bubble detachment on aerophilic surfaces, a series of fascinating aerophilic electrode strategies have been proposed. For example, Cui *et al.* developed an alveoli-mimicking polyethylene (PE) pouch electrolyzer, realizing a "bubble-free" mode by directly releasing bubbles into the gas phase, effectively avoiding energy loss and exhibiting a lower overpotential and higher current density.[27] A superaerophilic/superaerophobic (SAL/SAB) cooperative electrode has been proposed to induce bubble movement from the superaerophobic region (catalytic sites) to the superaerophilic region (gas collection sites).[28] In a breakthrough, Li *et al.* also proposed and conceptualized a rose-petal-effect-mimetic (RPEM) (a combination of superaerophilicity and high adhesion) design strategy to realize bubble-less and ampere-level HER and OER, and further realize efficient membrane-less water electrolysis.[29] These strategies not only provide new perspectives for rapid bubble removal and transport, but also open up new avenues for bionic structural engineering applications. However, the high-adhesion surface may induce a thick gas film, which can reduce charge transfer efficiency and block the reactive species from contacting the electrode, thus reducing the electrolysis efficiency. Therefore, it is desirable but challenging to design an electrode surface that can control unidirectional bubble transportation without the need for chemicals to deal with high bubble adherence.

Herein, taking water electrolysis as a probe reaction, we propose a tilted micro-cone array (TMCA) electrode for membrane-less electrolysis, which has tilted needle-like structures that can collect bubbles with unidirectional movement.[30,31] The TMCA electrode surface is modified with low lateral adhesion and moderate vertical adhesion, that is, a slippery state (Fig. 1c). Through these synergetic features, the TMCA electrode can manipulate the unidirectional transportation of bubbles in a "rolling-up" manner,[32,33] rather than the conventional severely adhered gas film, enabling the spontaneous >99.99% gas separation of bubbles at 1.5 mm distance and 240 mA cm^{-2} current. This work demonstrates the importance of the accurate manipulation of bubble transformation on electrodes and

provides a new opportunity for achieving spontaneous gas transportation in membrane-less electrolysis.

Results and discussion

Electrode fabrication

Fig. 2a shows the fabrication process for the electrode. In order to create the electrode template, a resin with a slanted micro-cone array was printed using a 3D printer with a resolution of 10 μm (Fig. 2a and Fig. S1, ESI†). At this point (stage I in Fig. 2a), the cones are spaced out across the substrate (1 cm × 1 cm) at intervals (s) of roughly 200 μm. Cones with a bottom radius (R) of 150 μm and an apex angle (α) of roughly 20° are shown in Fig. 2b and Fig. S2 (ESI†); the tilting angle (β) of the cones is controllable from 10° to 60° by altering the model source file (the effect of this on bubble transportation will be described later). Stage II in Fig. 2a depicts the pre-coating of the resin with an Ni–P conductive layer catalyzed by the deposited Pd nanoparticles (for additional information, see the experimental procedures). The resulting electrode was further electrodeposited with a Cu layer (step III in Fig. 2a), by adjusting the morphology *via* the deposition conditions, which in turn impacts surface wettability and consequent bubble transportation (Fig. S3, ESI†). As a result of Cu electrodeposition, the electrode becomes crimson. An ultrathin layer of catalyst Pt nanoparticles was deposited on the obtained Cu surface to endow it with HER activity (step IV in Fig. 2a), and there is no obvious variation in wettability after Pt deposition. Element mapping (Fig. 2d) demonstrates that the electrode has a uniform distribution of Cu and Pt species. Its high conductivity for electrochemical processes after metal loading is confirmed by the Nyquist curve (Fig. S4, ESI†), which demonstrates a low resistance of ~0.82 Ω. It is important to note that the structure of the micro-cone array with a certain tilting angle, resembling the spines of a cactus, was well retained during the above electrode manufacturing procedure (Fig. 2c).

Electrode surface engineering

The hydrogen evolution reaction (HER) in 0.5 M H_2SO_4 was used as a probe reaction to demonstrate the unique character of the prepared TMCA electrode with a special biomimetic structure. To ensure the effective unidirectional transport of the H_2 bubbles (from the tip to the root along the tilted cone-shaped array electrodes), the lateral adhesion (hysteresis resistance, f_H)[34,35] becomes a crucial factor for bubble movement. f_H is basically determined by the contact angle and the contact angle hysteresis (δ, namely "$\theta_a - \theta_r$"), expressed as[35]

$$f_a = 2\gamma \sin\left(\theta_{ms} + \frac{\delta}{4}\right)\sin\left(\frac{\delta}{4}\right)$$

or

$$f_r = 2\gamma \sin\left(\theta_{ms} - \frac{\delta}{4}\right)\sin\left(\frac{\delta}{4}\right),$$

where γ is the surface tension of water, θ_r and θ_a are the receding and advancing angles and θ_{ms} are the mean values of θ_r and θ_a, respectively. Thus, tailoring of the surface wettability of the TMCA electrode also turns out to be important for governing f_H.

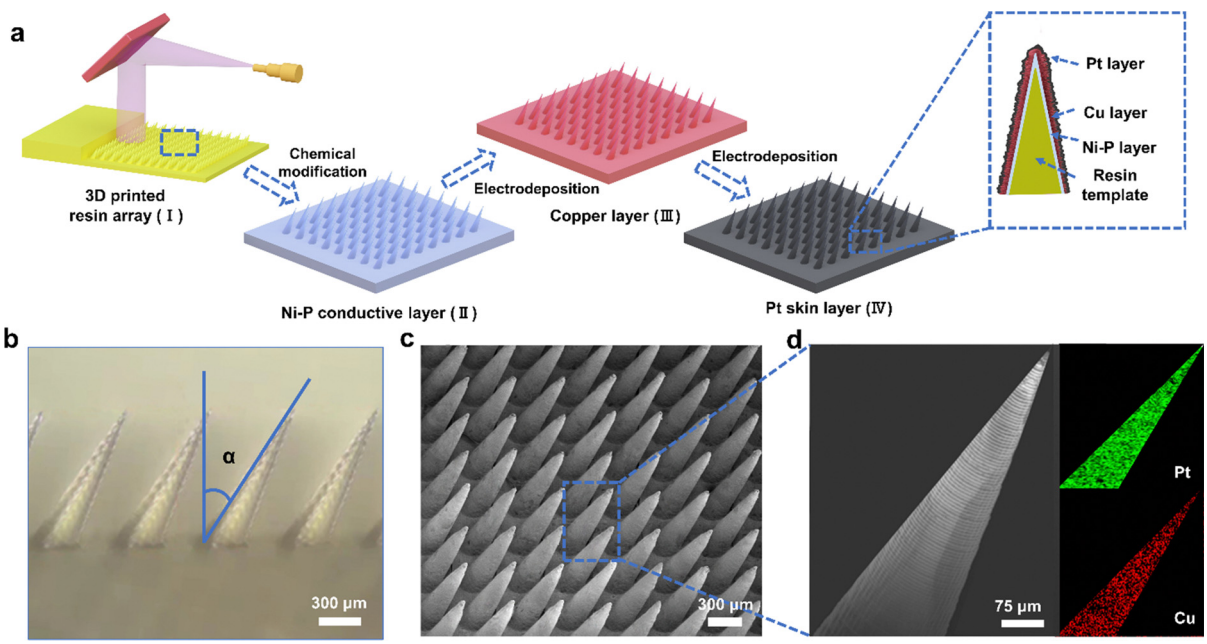

Fig. 2 Fabrication process of TMCA electrode. (a) Schematic illustration of the fabrication process of the tilted micro-cone array (TMCA) electrode (3D printed resin template → Ni–P conductive layer → electrodeposited copper layer → electrodeposited Pt skin layer); inset, cross-section of micro-cone array. (b) Side-view image of the tilted (α) substrate fabricated *via* 3D printing and surface plating, (c) scanning electronic microscopy (SEM) image of the as-prepared TMCA electrode, and (d) the magnified SEM image of a single cone and the corresponding elemental mapping, demonstrating the uniform coating of Pt and Cu elements.

Between steps II and III (Fig. 2a), the surface roughness can be controlled by electrodepositing various amounts of Cu, allowing for fine-tuning of the wettability.[36] The smooth electrode surface with slight modification by PTFE (without electrodeposited Cu) demonstrates aerophilicity with a bubble contact angle (CA) of 32°, exhibiting a Wenzel state (Fig. 3a, aerophilic, usually $<60°$), demonstrating its potential for use in aerophilic surface control.[37] As revealed by an adhesion force test (Fig. 3b; the detailed testing procedure is shown in Video S1, ESI†), such an aerophilic surface has a large adhesion force of 78 μN, and advancing (θ_a) and receding (θ_r) contact angles of 50° and 23°, respectively. By using a high-speed camera, we observed that H_2 bubbles are generated at the cone tips and move in a slipping manner towards the cone roots. However, the bubbles are easily trapped at the boundary between the cones as they move along the substrate and grow until their size is as large as approximately 300 μm (Fig. 3c), which might prevent the access of reagents to active sites, and hence reduce the catalytic efficiency.[37,38]

To avoid the excessive adhesion and inadequate stability observed in the above sample, we further modified the Cu layer to tune the surface wettability (voltage of −1 V for 1200 s) (Fig. 3d and Fig. S4, ESI†). The electrode surface showed superaerophobicity with a bubble CA of 165°, exhibiting a Cassie state (Fig. 3e, superaerophobic, usually $>140°$). With θ_a of 167° and θ_r of 162° (Fig. S5, ESI†), the adhesion force was measured to be as low as 3 μN, revealing a superaerophobic feature. As anticipated, the bubbles formed at the electrode tips exhibit high free detachment, and are well dispersed into the electrolyte in a random manner (Fig. 3f). Consequently, it is reasonable that the hydrogen (H_2) and oxygen (O_2) generated should readily intermix in membrane-less electrolysis.

Based on the above findings, we tried to engineer the electrode surface with moderate vertical adhesion, to avoid premature detachment of bubbles (particularly at the tip area), and accumulation of bubbles at the cone roots. For this purpose, by controlling the surface roughness *via* electrodeposition of Cu under optimized conditions (voltage of −2 V for 600 s, ~35 μm), we fabricated an electrode with a surface consisting of pine-needle-like cones with a bubble CA of 130° (Fig. 3g), an indication of an aerophobic feature. An adhesion force with a moderate value of 16 μN was obtained, together with θ_a of 135° and θ_r of 127° (Table S4, ESI†), indicating the low lateral adhesion force and moderate vertical adhesion force of the electrode surface, which we define as a slippery aerophobic (transition) state (Fig. 3h). This is mainly due to the fact that the pine-needle-like arrays with moderate electrodeposition time had an appropriate structural depth and roughness, allowing the partial penetration of the bottom of the bubble into the gap.

According to the sine function of f_H, small contact angles corresponding to the aerophilic property of the electrode and large contact angles corresponding to the aerophobic property

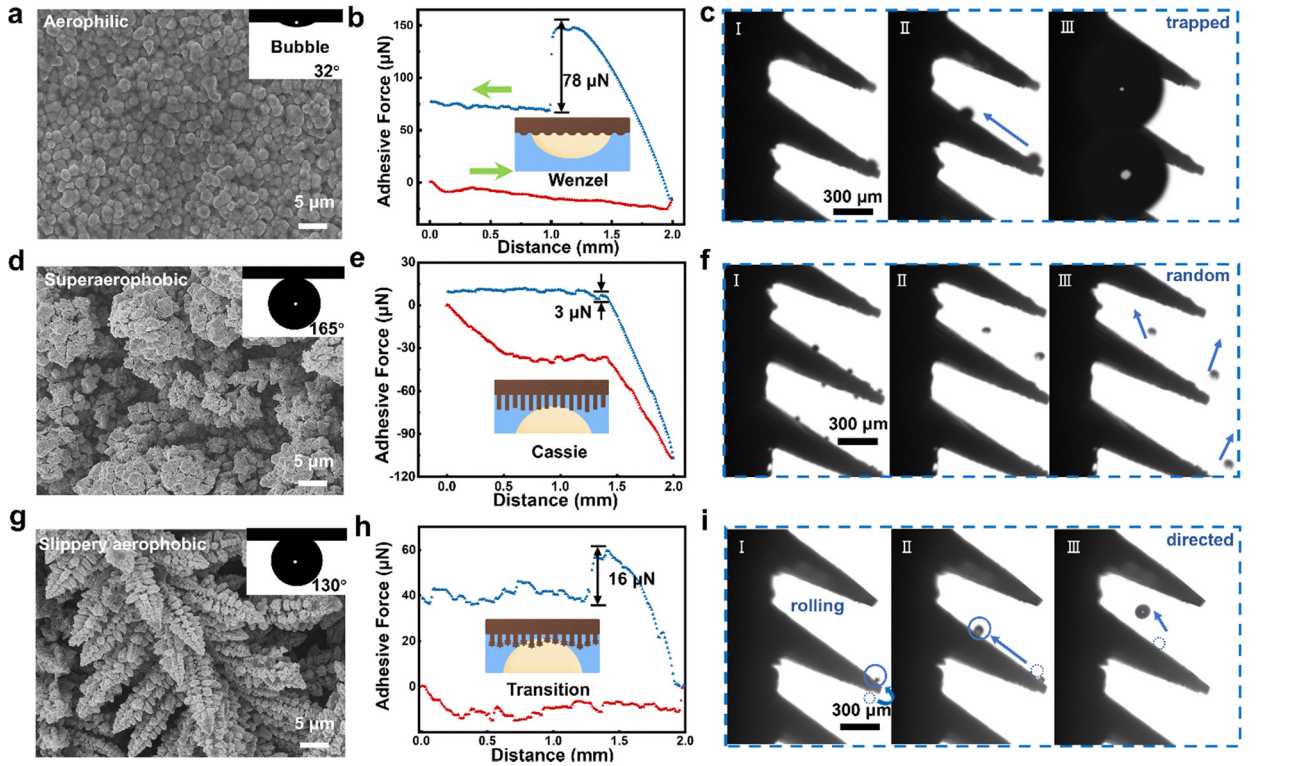

Fig. 3 Influence of electrode wettability on bubble transportation behavior. SEM images of the surface of (a) aerophilic, (d) superaerophobic, and (g) slippery aerophobic electrodes (the inset images depict the respective bubble contact angles). The adhesion force curves at the surface of (b) aerophilic, (e) superaerophobic, and (h) slippery aerophobic electrodes (the inset pictures show schematic diagrams of the respective wetting states). The bubble behaviors on different electrodes: (c) trapped in aerophilic ones, (f) escaping from superaerophobic ones, and (i) rolling-up on slippery aerophobic electrodes.

of the electrode would both lead to a low enough f_H for bubble movement. As demonstrated above, the aerophilic property would induce serious bubble trapping and blockage of active sites, while the superaerophobic property would induce random detachment. With the aerophobic property and a finely controlled adhesion force, we define the surface features of a "slippery aerophobic" surface. By employing this electrode, we found that the initially generated tiny bubbles could roll up from the lower tip position to the upper side without premature detachment and move further towards the cone root with relatively low lateral adhesion for movement (Fig. 3i). The bubbles might detach from the electrode surface during rolling-up, when the driving force for detachment was greater than the adhesion force (F_A). It is notable that these detached bubbles mostly meet the upper cones, continue their flipping and coalescence, ensuring their unidirectional motion to the roots.

The influence of tilting angle

Besides surface wettability, we expect that the tilting angle (α) of the cones on the electrode may also play an important role in the transportation and detachment of bubbles, as well as the catalytic performance. For this purpose, we prepared a series of electrodes composed of micro-cones with different tilting angles (α, ranging from 10° to 60°). The images and movies of bubble transportation and detachment on the upper surface (bubbles on the undersurface would flip to the upper surface) were recorded, and the results for α from 10° to 60° are displayed in Fig. 4a–c and Fig. S6 and 7 and Movies S2–S8 (ESI†). According to the statistical results (Fig. 4d), the start-up (from the pinning state to the rolling-up state) diameters and rolling speed of the generated bubbles increase as the tilting angle increases. Specifically, as the tilting angle (α) increases from 10° to 60°, the average start-up diameter of the bubbles decreases from 37 ± 3 μm (α = 10°) to 16 ± 4 μm (α = 50°), 13 ± 3 μm (α = 60°); and the rolling speed of the bubbles increases from 4 ± 2 cm s^{-1} (α = 10°) to 25 ± 3 cm s^{-1} (α = 50°), and 37 ± 3 cm s^{-1} (α = 60°), which is quite a considerable change in comparison to related studies,[39,40] revealing the rapidity of the bubble motion. Accordingly, the bubble size for detachment decreases from 150 ± 10 μm (α = 10°) to 38 ± 2 μm (α = 50°), but then increases to 78 ± 2 (α = 60°). We also measured the residence time for bubbles on the cone, going from generation to detachment, showing that it decreases from 265 (α = 10°) to 18 ms (α = 50°), but then increases to nearly 80 ms (α = 60°) (Fig. 4e and Fig. S8, ESI†). This is due to the decreasing inter-cone space as the tilting angle increases, so generated bubbles would be easily trapped there when α is greater than 60° (Fig. S9 and Movie S9, ESI†). Thus, a tilting angle of 50° is regarded as optimal, allowing the generated bubbles to be transported rapidly without being trapped, which would be beneficial to the performance.

Force analysis for rolling bubble

To better understand why bubbles are transported in one direction on the tilted micro-cone array electrode, we performed a

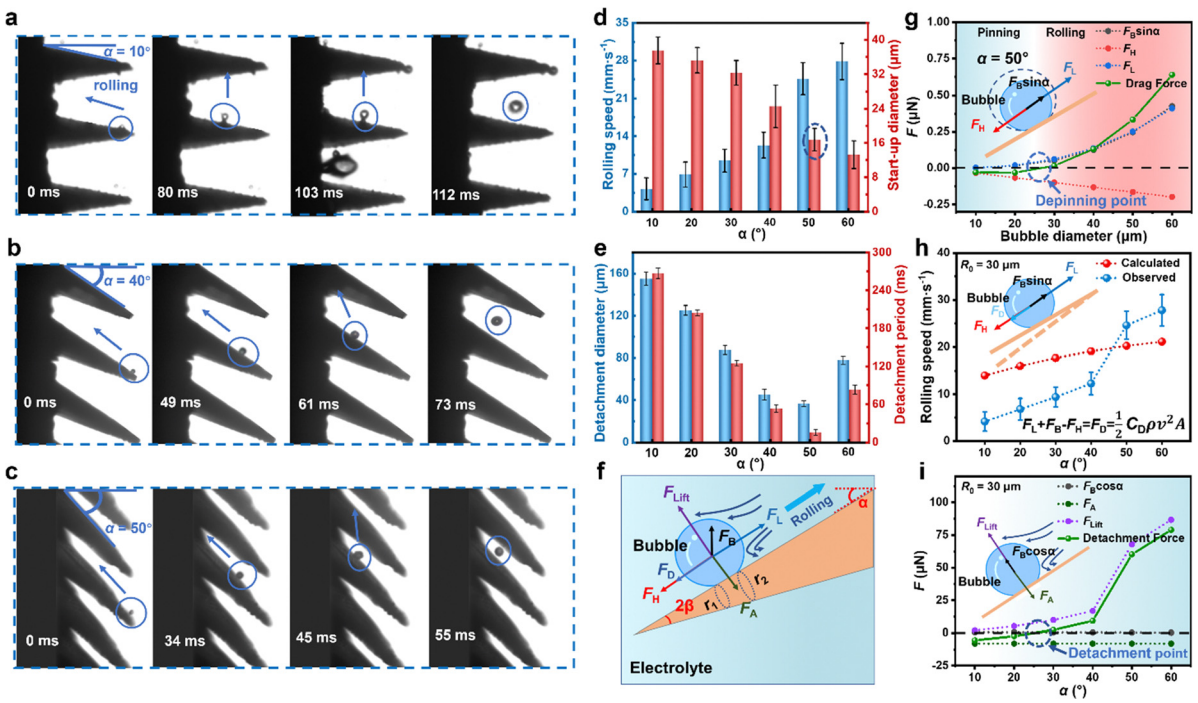

Fig. 4 Influence of tilting angle on bubble transportation behavior. Typical bubble transport behaviors with different tilting angles of (a) α = 10°, (b) α = 40°, and (c) α = 50°. The experimental statistics of (d) rolling speed and start-up diameter of rolling bubbles, and (e) the detachment diameter and lifetime of the bubbles. (f) Schematic illustration of force analysis of a rolling bubble. (g) The force analysis curve for the start-up diameter of rolling bubbles at α = 50° (the inset figures show the schematic force analysis). (h) Comparison of calculated and observed rolling speeds, and (i) detachment force analysis curves of a given bubble (R_0 = 30 μm) rolling on cones with different tilting angles (the inset figure represents the schematic force analysis).

systematic force analysis for a rolling bubble (Fig. 4f). This mainly involved the asymmetric shape-induced Laplace pressure F_L, buoyancy F_B and adhesion force F_A of the bubble. As it moves, the bubble faces hysteresis resistance F_H, water resistance F_D, shearing-action-induced lifting force F_{Lift} and adhesion force F_A.

In detail, the Laplace pressure F_L can be expressed as,[36,41]

$$F_L = 2\gamma\left(\frac{1}{r_1} - \frac{1}{r_2}\right) S \sin\beta \quad (1)$$

where r_1 and r_2 are the local radius of the bubbles on the front side and rear side, respectively, γ is the surface tension of the water, and S is the bubble/electrode interfacial area (Tables S1 and S2, ESI†). F_B is proportional to the volume of the bubble. Thus, for a given tilting angle of 50°, the drag force is determined by the combined interactions of driving forces (schematic diagram shown in Fig. 4g and Table S3, ESI†). As calculated, F_L and F_B both increase cubically as functions of bubble size. Eventually, as the drag force overcomes resistance, the generated bubbles go from the static pinning state into a rolling state, at a critical value of *ca.* 22 μm for α = 50° (Fig. 4g), which is nearly the same as the observed start-up diameter of 16 ± 4 μm in Fig. 4d (marked by a blue oval), and *vice versa* for other tilting degrees. In addition to the bubble size effect, bubble movement is also sensitive to variation in the tilting angle α, as shown in Fig. S10 (ESI†). For a given bubble (R_0 = 30 μm) rolling on a tilted surface, the velocity-dependent water resistance F_D would balance with the drag force, which is determined from $F_B \sin\alpha$, F_L, and F_H ($F_D = F_B \sin\alpha + F_L + F_H$), expressed as

$$\frac{1}{2} C_D \rho_l v^2 A,$$

where C_D and ρ_l are the drag coefficient and water density, respectively, v is the speed and A is the cross-sectional area of the rolling bubble. When α increases from 10° to 60°, the drag force would increase with the main contribution of $F_B \sin\alpha$. Assuming that the forces are balanced at this point, F_D balanced with $F_B \sin\alpha + F_L + F_H$ will then increase, and thereby the rolling speed v increases correspondingly, coinciding with the observed increasing trend (Fig. 4d and Fig. S11, ESI†). The calculation confirms the importance of bubble size and tilting angle of micro-cones for the efficiency of unidirectional transportation.

The detachment of bubbles is determined by the normal component of buoyancy $F_B \cos\alpha$, which would decrease with increasing tilting angle, causing the shearing action-induced lifting force F_{Lift} to become dominant (Fig. 4i). Specifically, the previously mentioned water resistance would also induce the shearing action along the top and the bottom parts of the bubbles, and bring about a lifting force F_{Lift} owing to the asymmetric flow over the top and bottom parts with Bernoulli suction, which can be mainly expressed as

$$F_{Lift} = \frac{1}{4} C_L \frac{w}{R_0} \rho A v^2$$

where C_L is estimated as 1.375 according to Bernoulli's equation and potential flow theory. The adhesion force F_A that prevents the bubble from detaching can be represented as

$$\gamma 2\pi (R_0 \sin\theta) \sin\theta,$$

where θ is the intrinsic contact angle on a smooth surface, which is essentially unchanged for a given bubble and surface (dark green dashed line).[42–44] As a result, with increasing tilting angle, the rolling speed increases, and F_{Lift} increases accordingly, promoting the net force for bubble detachment (green solid line), which is also in accordance with the observed decreasing trend in detachment diameter and period of the bubbles (Fig. 4e). Meanwhile, some of the generated tiny bubbles can be passively removed in advance due to the coalescence effect, which further reduces the effective bubble detachment size.

Hydrogen evolution reaction performance

The tilting angle effect (from 10° to 60°) was also verified with HER performance, as shown in Fig. 5a. Notably, all the curves begin at similar initial potentials (~50 mV) due to the loading of uniformly loaded Pt catalysts, but the rates at which the current density increase vary significantly, with superior performance at 50°. Similarly, the 50° tilting angle also tops the current density after the normalization based on the measured double-layer capacitances (Fig. 5b and Fig. S12a and S11, ESI†), due to the enhancement in bubble conveyance, which is clearly visible in the frontal view with bubbles swiftly navigating through the conical gaps (Movie S10, ESI†); and the current density also begins to decline for α larger than 60°. The corresponding ECSA normalized current density decreases from 26.7 mV dec^{-1} to 19.3 mV dec^{-1} as α increases from 10° to 50°, and increases to 29.3 mV dec^{-1} when α = 60° (Fig. S12b, ESI†). This increase can be attributed primarily to the excessive tilting angle (60°), which would cause bubble trapping between the two neighboring cones. In the case of α = 60°, the subsequent small bubbles would continually merge into the trapped bubble, leading to inverse expansion toward the cone tip and thereby a severe bubble shielding effect (Fig. S9, ESI†). To further verify this phenomenon, we carried out electrochemical performance tests and bubble behavior observations on TMCA electrodes with different cone spacings (R = 75/300 μm) and smaller cone densities (D = 400 μm), as shown in Fig. S12 and S13 (ESI†). Compared to the TMCA electrode with a 50° tilting angle, the electrode with a larger cone spacing ($R_{75}D_{200}$) performs poorly at high current, because the conic angle 2β is too low to provide sufficient Laplace driving force, causing bubbles to adhere to the electrode surface instead of moving along the cone (Fig. S14a, ESI†). The electrode with a smaller cone spacing ($R_{300}D_{200}$) suffers from severe bubble shielding, similar to the electrode with a 60° tilting angle (Fig. S14b, ESI†), resulting in significant current fluctuations. The electrode with a smaller cone density ($R_{150}D_{400}$) exhibits decreased performance due to the reduced reaction area (Fig. S14c, ESI†). The results further demonstrate the important role of electrode structure in promoting mass transfer and electrochemical performance. Additionally, we achieved a durability experiment with a limited increase of 22 mV in potential over 90 hours (Fig. S15, ESI†).

For a proof of concept, based on the above knowledge of manipulation and understanding of bubble transportation, we

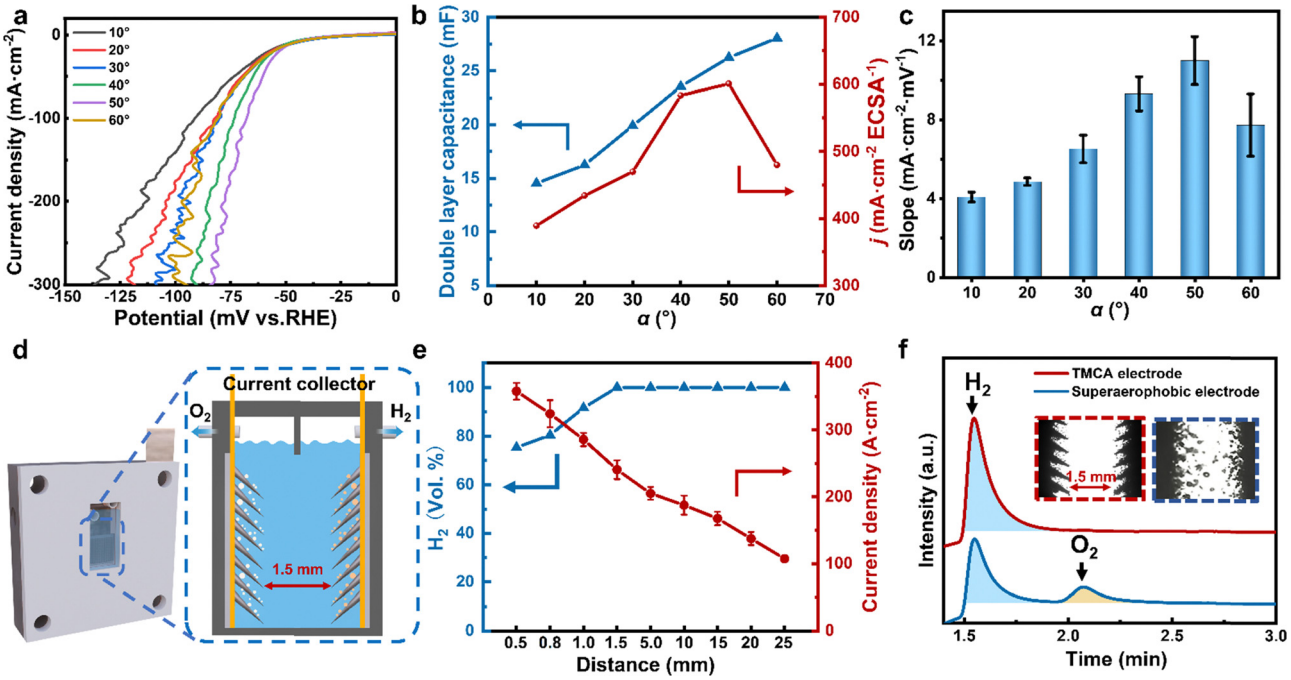

Fig. 5 The electrocatalytic performance of the TMCA electrode for water electrolysis. (a) IR-corrected LSV curves of different tilting angles. (b) Double layer capacitance and ECSA normalized current density curves for HER in 0.5 M H_2SO_4 of different tilting angles. (c) The corresponding current increasing rates of different tilting angles. (d) Scheme of a dual-electrode device with a working distance of 1.5 mm (the inset images depict the corresponding schematic illustration of the bubble evolution process and the magnified configuration of the two electrodes). (e) Inter-electrode distance-dependent current densities and variation in gas purity. (f) Gas chromatogram of the product hydrogen based on the tilted array electrodes (red line), and ordinary no-cone superaerophobic electrodes (blue line) (the inset figures are snapshots of the bubble evolution process with the TMCA electrode and the traditional superaerophobic electrodes).

fabricated a membrane-less water electrolysis device with integrated bubble generation and collection functions, using an anode (Ir) and cathode (Pt) with tunable working distance, aiming for high product purity and large current density with our electrode design (Fig. 5d and Fig. S16, ESI†). *In situ* microscopy observation of the spacing electrolyte (Fig. 5f inset) reveals that, in contrast to the absence of radical bubbles between TMCA electrodes (Movie S11, ESI†), conventional planar superaerophobic electrodes (Movie S12, ESI†) exhibit vigorous irregular bubble movement. To reduce the ohmic impedance and enhance the current density, we investigated the dependency of current density on electrode gap distance. In order to achieve a high current density in membrane-less electrolysis systems, it is necessary to decrease the working distance between the electrodes (as shown in Fig. 5e), which increases from 107 to 357 mA cm^{-2} when the electrode distance decreases from 35 to 0.5 mm. The systematic analysis reveals that a distance of only 1.5 mm is suitable for working with the two TMCA electrodes. Such an electrode separation permits a current density of 240 mA cm^{-2}. The chromatogram findings further demonstrate that the purity of the collected H_2 gas product is as high as 99.99%, demonstrating the effectiveness of the electrode surface engineering in preventing gas mixing in the electrolyzer without the use of a membrane at such a short electrode distance. In contrast, the H_2 purity of the conventional planar superaerophobic electrodes at the same distance is only 88.3% (Fig. 5f and Fig. S17, ESI†). Therefore, compared to the commonly used strategies mentioned above (wettability or shape gradient based on aerophilic electrodes) for high-gas-purity membrane-less electrolysis, the biomimetic TMCA electrode can achieve a brand new "rolling" manner for high-efficiency unidirectional bubble transportation with a rather limited inter-electrode working distance, achieving high performance for various gas evolution reactions. Another interesting feature is that the gas generation/collection functions are realized by the hierarchical structure alone, without the use of wettability-modifying additives (such as PTFE or SiO_2 channels) that could limit their practical applicability.

Conclusions

In summary, we have successfully developed a biomimetic downward-tilted micro-cone array electrode featuring a slippery aerophobic surface. This electrode demonstrates exceptional performance in facilitating unidirectional bubble evolution for membrane-less electrolysis. Notably, it achieves complete separation of the H_2/O_2 product even when the distance between the two gases is as tiny as 1.5 mm. In contrast to the conventional phenomenon of random bubble detachment into the electrolyte, this approach enables the controlled movement of bubbles in a unidirectional manner along the electrode with a relatively small size. The driving forces are identified as Laplace pressure and buoyancy. The purity of the gas product,

achieved through the utilization of two slanted array electrodes with a working distance of 1.5 mm, demonstrates exceptional gas product collecting capabilities, with a purity exceeding 99.99% at a current density of 240 mA cm^{-2}. The proposed methodology should serve as a source of inspiration for the development of electrode designs in the context of membraneless electrolysis.

Data availability

Data available with the paper or ESI:† the authors declare that the data supporting the findings of this study are available within the paper and its ESI,† files. Should any raw data files be needed in another format they are available from the corresponding author upon reasonable request. Source data are provided with this paper.

Conflicts of interest

There are no conflicts to declare.

Acknowledgements

This work was supported by the Natural Science Foundation of China (No. 21935001, 22325805, 21978147, 22379005), National Key Research and Development Project (2022YFA1504000), Beijing Natural Science Foundation (No. Z210016, JQ22003), Long-term subsidy mechanism from the Ministry of Finance and the Ministry of Education of PRC.

References

1 Z. Y. Wang, L. Xu, F. Z. Huang, L. B. Qu, J. T. Li, K. A. Owusu, Z. Liu, Z. F. Lin, B. H. Xiang, X. Liu, K. N. Zhao, X. B. Liao, W. Yang, Y. B. Cheng and L. Q. Mai, *Adv. Energy Mater.*, 2019, **9**, 1900390.
2 A. Tasaka, *J. Fluorine Chem.*, 2007, **128**, 296–310.
3 K. R. Yang, N. N. Han, Z. Y. Lu, Y. J. Li, W. W. Xu, T. F. Gao, Y. Z. C. Zhao, V. S. Batista, W. Liu and X. M. Sun, *Nat. Commun.*, 2018, **9**, 924.
4 X. Y. Yan, J. Biemolt, K. Zhao, Y. Zhao, X. J. Cao, Y. Yang, X. Y. Wu, G. Rothenberg and N. Yan, *Nat. Commun.*, 2021, **12**, 4143.
5 A. Manzotti, E. Quattrocchi, A. Curcio, S. C. T. Kwok, M. Santarelli and F. Ciucci, *Energy Convers. Manage.*, 2022, **254**, 115156.
6 B. Rausch, M. D. Symes, G. Chisholm and L. Cronin, *Science*, 2014, **345**, 1326–1330.
7 W. G. J. Van Helden, C. W. M. Van Der Geld and P. G. M. Boot, *Int. J. Heat Mass Transfer*, 1995, **38**, 2075–2088.
8 S. Kim, T. Kim, S. Lee, S. Baek, T. Park and K. Yong, *Adv. Mater.*, 2017, **29**, 1702431.
9 C. Zhang, W. Zhang, N. E. Drewett, X. Y. Wang, S. J. Yoo, H. X. Wang, T. Deng, J. G. Kim, H. Chen, K. K. Huang, S. H. Feng and W. T. Zheng, *ChemSusChem*, 2019, **12**, 1000–1010.
10 C. M. Yu, P. P. Zhang, J. M. Wang and L. Jiang, *Adv. Mater.*, 2017, **29**, 1703053.
11 N. Li, C. Huang, X. Wang, Y. Feng and J. An, *Chem. Eng. J.*, 2022, **450**, 138246.
12 Y. Zhou, N. Jin, Y. Ma, Y. Cui, L. Wang, Y. Kwon, W.-K. Lee, W. Zhang, H. Ge and J. Zhang, *Adv. Mater.*, 2023, **35**, 2209500.
13 D. Zhou, P. Li, X. Lin, A. McKinley, Y. Kuang, W. Liu, W.-F. Lin, X. Sun and X. Duan, *Chem. Soc. Rev.*, 2021, **50**, 8790–8817.
14 J. K. Zhang, F. Y. Dong, C. Q. Wang, J. M. Wang, L. Jiang and C. M. Yu, *ACS Appl. Mater. Interfaces*, 2021, **13**, 32435–32441.
15 Z. Y. Long, Y. Y. Zhao, C. H. Zhang, Y. H. Zhang, C. M. Yu, Y. C. Wu, J. Ma, M. Y. Cao and L. Jiang, *Adv. Mater.*, 2020, **32**, 1908099.
16 J. Li and Z. G. Guo, *Research-China*, 2019, **2019**, 9139535.
17 J. L. Song, Z. A. Liu, X. Y. Wang, H. Liu, Y. Lu, X. Deng, C. J. Carmalt and I. P. Parkin, *J. Mater. Chem. A*, 2019, **7**, 13567–13576.
18 X. S. Wang, H. Y. Bai, J. R. Yang, Z. Li, Y. C. Wu, C. M. Yu, L. Jiang and M. Y. Cao, *Small*, 2021, **17**, 2007803.
19 K. Han and K. Yong, *Adv. Funct. Mater.*, 2021, **31**, 2101970.
20 Z. Shang, Y. Zhang, L. Luo, C. Cheng, T. Xie, F. Chen, S. Sheng, Y. Kuang, W. Liu, H. Xu and X. Sun, *Sci. China Mater.*, 2021, **64**, 892–898.
21 S. Feng, J. Delannoy, A. Malod, H. Zheng, D. Quéré and Z. Wang, *Sci. Adv.*, 2020, **6**, eabb4540.
22 X. Li, J. Zhang, X. Wang, D. Lv, C. Cao, L. Ai and X. Yao, *Droplet*, 2022, **1**, 65–75.
23 X. Xiao, C. H. Zhang, H. Y. Ma, Y. H. Zhang, G. L. Liu, M. Y. Cao, C. M. Yu and L. Jiang, *ACS Nano*, 2019, **13**, 4083–4090.
24 P. Guo, Z. B. Wang, L. P. Heng, Y. Q. Zhang, X. Wang and L. Jiang, *Adv. Funct. Mater.*, 2019, **29**, 1808717.
25 C. M. Yu, X. B. Zhu, K. Li, M. Y. Cao and L. Jiang, *Adv. Funct. Mater.*, 2017, **27**, 1701605.
26 X. Tang, H. R. Xiong, T. T. Kong, Y. Tian, W. D. Li and L. Q. Wang, *ACS Appl. Mater. Interfaces*, 2018, **10**, 3029–3038.
27 J. Li, Y. Zhu, W. Chen, Z. Lu, J. Xu, A. Pei, Y. Peng, X. Zheng, Z. Zhang, S. Chu and Y. Cui, *Joule*, 2019, **3**, 557–569.
28 C. Zhang, Z. Xu, N. Han, Y. Tian, T. Kallio, C. Yu and L. Jiang, *Sci. Adv.*, 2023, **9**, 6978.
29 K. Deng, H. Feng, Y. Zhang, D. Liu and Q. Li, *Joule*, 2023, **7**, 1852–1866.
30 D. Wang, Q. Sun, M. J. Hokkanen, C. Zhang, F. Y. Lin, Q. Liu, S. P. Zhu, T. Zhou, Q. Chang, B. He, Q. Zhou, L. Chen, Z. Wang, R. H. A. Ras and X. Deng, *Nature*, 2020, **582**, 55–59.
31 V. Jokinen, E. Kankuri, S. Hoshian, S. Franssila and R. H. A. Ras, *Adv. Mater.*, 2018, **30**, 1705104.
32 H. Li, T. Yan, K. A. Fichthorn and S. Yu, *Langmuir*, 2018, **34**, 9917–9926.
33 Y. Pi, Q. Shao, P. Wang, J. Guo and X. Huang, *Adv. Funct. Mater.*, 2017, **27**, 1700886.
34 C. M. Yu, M. Y. Cao, Z. C. Dong, J. M. Wang, K. Li and L. Jiang, *Adv. Funct. Mater.*, 2016, **26**, 3236–3243.
35 J. Qin, D. Zhou, B. Shi, F. Chen, L. Luo, A. Kumar, C. Wang, X. Lin, S. Sheng, W. Xu, Z. Shang, C. Cheng, Y. Kuang,

W.-F. Lin, H. Xu and X. Sun, *Langmuir*, 2020, **36**, 11422–11428.
36 C. M. Yu, M. Y. Cao, Z. C. Dong, K. Li, C. L. Yu, J. M. Wang and L. Jiang, *Adv. Funct. Mater.*, 2016, **26**, 6830–6835.
37 R. Iwata, L. Zhang, K. L. Wilke, S. Gong, M. He, B. M. Gallant and E. N. Wang, *Joule*, 2021, **5**, 887–900.
38 P. A. Kempler, R. H. Coridan and N. S. Lewis, *Energy Environ. Sci.*, 2020, **13**, 1808–1817.
39 Y. Yan, Q. Zhang, Y. Li, Z. Guo, D. Tian, X. Zhang and L. Jiang, *J. Mater. Chem. A*, 2020, **8**, 8605–8611.
40 C. Brownlee, *ACS Nano*, 2019, **13**, 4–7.
41 X. Z. Xue, C. M. Yu, J. M. Wang and L. Jiang, *ACS Nano*, 2016, **10**, 10887–10893.
42 Z. Lu, W. Zhu, X. Yu, H. Zhang, Y. Li, X. Sun, X. Wang, H. Wang, J. Wang, J. Luo, X. Lei and L. Jiang, *Adv. Mater.*, 2014, **26**, 2683–2687.
43 Y. Wang, L. Zhang, Y. Guo, Y. Gan, G. Liu, D. Zhang and H. Chen, *Small*, 2021, **17**, 2103423.
44 M. Li, P. Xie, L. Yu, L. Luo and X. Sun, *ACS Nano*, 2023, **17**, 23299–23316.